A R C H I V E S O F M E T A L L U R G Y A N D M A T E R I A L S
Volume 59 2014 Issue 1
DOI: 10.2478/amm-2014-0034

W. WOŁCZYŃSKI*, C. SENDEROWSKI**, J. MORGIEL*, G. GARZEŁ*

D-GUN SPRAYED Fe-Al SINGLE PARTICLE SOLIDIFICATION

KRYSTALIZACJA POJEDYNCZEJ CZĄSTKI Fe-Al NANIESIONEJ METODĄ DETONACYJNĄ

Some Fe-Al particles less than 50 μm in diameter were deposited onto the steel substrate by means of the D-gun spraying. A solidification mechanism of an individual particle is described. The particle subjected to the description contained nominally 63 at.% Al. The description was preceded by the TEM / SAED analysis of both the Fe-Al coating and Ni-20Cr interlayer. The whole number of the analyzed particles was partially melted during the deposition. The solidification products like: amorphous phase sub-layer, oscillatory sub-layer which contains two types lamellae distributed alternately and typically non-equilibrium phase sub-layer were revealed. In the micro scale, solidification was considered as a process which occurred in two directions: towards the substrate and towards the non-melted particle part. Both solidification processes underwent the positive thermal gradients. The boron addition was localized within the eutectic precipitates pushed and then rejected by the solid/liquid interface of the solidifying non-equilibrium phase. The proposed model is a general one and therefore can be applied to other systems description.

Keywords: Fe-Al coating, Ni-20Cr interlayer, rapid solidification, D-gun spraying, boron localization, competitive growth of phases

Cząstki proszku Fe-Al mniejsze niż 50 μm w średnicy zostały osadzone detonacyjnie na podłożu stalowym. Opisuje się mechanizm krystalizacji pojedynczej cząstki. Cząstki poddane opisowi zawierały nominalnie 63 at.% Al. Opis poprzedzono badaniami struktury metodą TEM / SAED dotyczącymi zarówno powłoki Fe-Al jak i międzywarstwy Ni-20Cr. Wszystkie analizowane cząstki były częściowo nadtopione podczas osadzania. Zidentyfikowano produkty krystalizacji takie jak: podwarstwę amorficzną, podwarstwę oscylacyjną zawierającą periodycznie ułożone płytki dwu faz oraz podwarstwę zawierającą fazę typowo nierównowagową. W mikroskali proces wzrostu faz jest analizowany jako zachodzący w dwu kierunkach: w stronę podłoża i w stronę niestopionej części cząstki. Obydwa procesy wzrostu zachodziły w obecności dodatniego gradientu temperatury. Bor dodany do powłoki został zlokalizowany w eutektyce odepchniętej przez front krystalizacji fazy typowo nierównowagowej. Proponowany model ma charakter ogólny i może być zastosowany do opisu innych systemów.

1. Introduction

The Fe-Al type protective coatings deposited onto the steel substrate evince very useful properties like good micro-hardness, adhesion, resistance to corrosion at high temperature, low porosity, resistance to abrasive wear, good lubricating abilities and tightness, [1-13]. However, industrial application the Fe-Al type coating is limited due to the poor ductility and fracture toughness. One of the possible way to improve these two properties is the grains boundaries strengthening by the addition of boron and zirconium. Moreover, mentioned elements improve the coating adhesion, [14].

Therefore, the microstructure analysis is required to determine the localization of boron and zirconium. Usually, it is satisfactory to deliver the TEM, SAED and X-ray (EDX) examinations, [15-17]. However, the detailed study of the coating formation is also necessary. The microstructure formation within the Fe-Al type protective coating with the boron and zirconium addition was already studied in the macro scale, [14]. Alas, there are no investigations on finer scale, that is, on the interplay between two neighbouring Fe-Al particles. Especially, the model for solidification of partially melted individual particle does not yet exist in the literature of the subject.

Usually, coating is partially melted because the temperature distribution inside the coating is not homogeneous, [18-19]. In the current paper, an attempt is made to show that the non-homogeneous temperature field exists in the micro scale, that is, inside a single particle. Thus, it is assumed that the particles are partially melted only, Fig. 1c, then subjected to the rapid solidification and different phases can be precipitated as some sub-layers situated across a given Fe-Al particle, Fig. 1d. The heterogeneity of temperature field inside a single particle results from the shock which appears at the substrate/particle interface when the particle is sprayed, Fig. 1a, Fig. 1b. The emitted heat is transferred into two direc-

* INSTITUTE OF METALLURGY AND MATERIALS SCIENCE, 25 REYMONTA STR., 30 059 KRAKÓW, POLAND
** MILITARY UNIVERSITY OF TECHNOLOGY, 2 KALISKIEGO STR., 00-908 WARSZAWA, POLAND

tions: towards steel substrate and towards non-melted part of particle, next to the air.

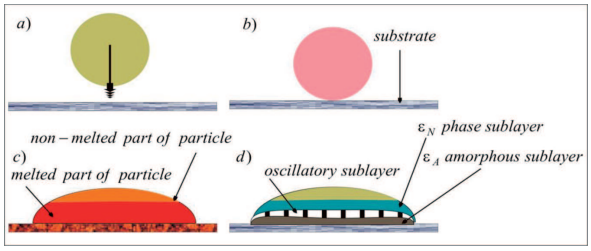

Fig. 1. D-gun spraying shown sequentially: a/ the Fe-Al particle moves towards the steel substrate, b/ the particle beats the substrate, c/ the particle becomes flattened and partially melted, d/ some sub-layers appear due to rapid solidification

2. Experiment

The Fe-40Al-0.05Zr at% + 50 ppm of B – powder made by Vacuum Inert Gas Atomization (VIGA) in CEA – Grenoble, France, with grain sizes ranging from 5 to 45 μm was used as a coating material, Fig. 2.

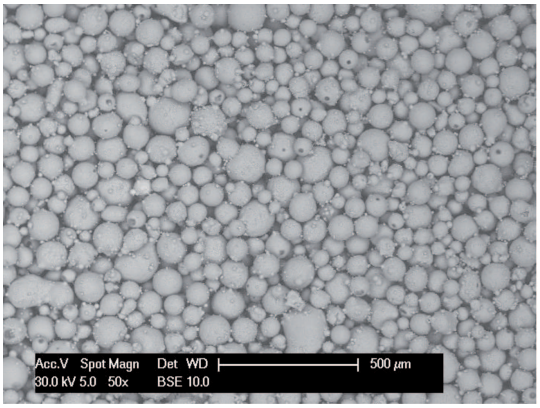

Fig. 2. The Fe-Al particles used in the D-gun spraying

The D-gun spraying of the Fe-Al coating was preceded by the D-gun deposition of the Ni-20Cr interlayer which is responsible for a satisfactory coating / substrate adhesion, Fig. 3.

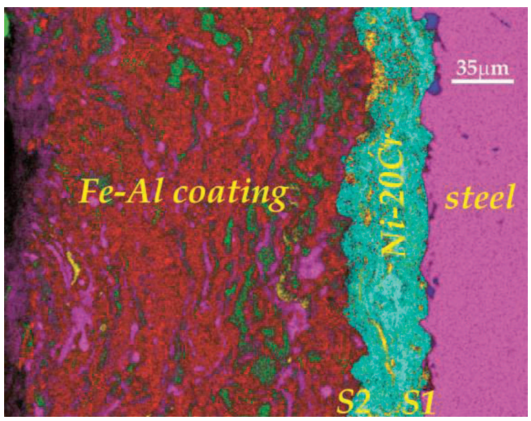

Fig. 3. Fe-Al coating and Ni-20Cr interlayer as deposited by the D-gun spraying on steel substrate; the marked S1, S2 - diffusion zones are: *S1=Fe/Ni/Cr*, *S2=Fe/Al/Ni/Cr*

A localization of Zr and B was first studied within the Ni-20Cr interlayer, Fig. 4.

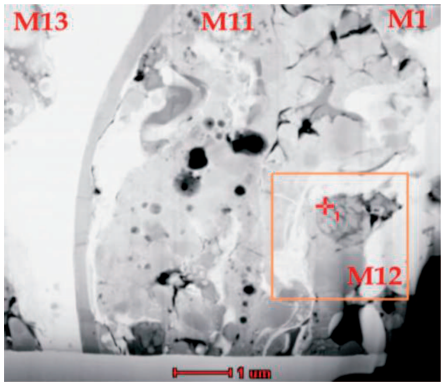

Fig. 4. The Ni-20Cr interlayer with distinguished areas subjected to the STEM study

The M1 area was localized in the steel substrate. However, the EDX analysis confirms the following distribution within the M11, M12 and M13 areas, Fig. 5-7.

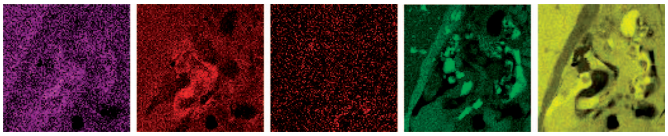

Fig. 5. The EDX analysis of the Ni-20Cr interlayer; **Zr**, **Fe**, **B**, **Cr**, **Ni** in the M11 area

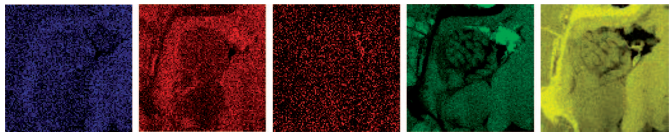

Fig. 6. The EDX analysis of the Ni-20Cr interlayer; **Zr**, **Fe**, **B**, **Cr**, **Ni** in the M12 area

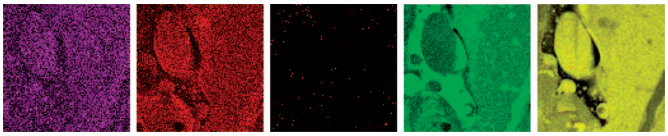

Fig. 7. The EDX analysis of the Ni-20Cr interlayer; **Zr**, **Fe**, **B**, **Cr**, **Ni** in the M13 area

There are not significant segregations of boron/zirconium within the studied areas according to the performed EDX analysis.

Additionally, the X-ray studies were applied to the Fe-Al sprayed coating, Fig. 8.

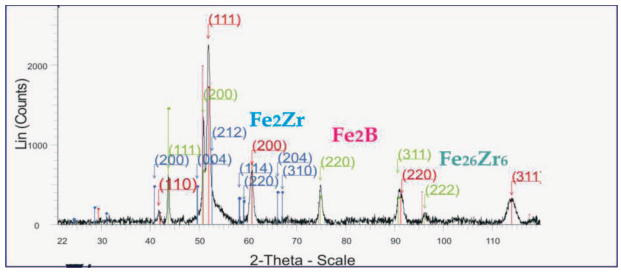

Fig. 8. X-ray identification of the Fe_2B, Fe_2Zr and $Fe_{26}Zr_6$ intermetallic compounds within the sprayed Fe-Al coating (colours of a given compound description correspond to the piques colour)

According to the result shown in Fig. 8, the Fe_2B intermetallic compound can be expected in the Fe-Al coating. On the other side, the Fe_2B compound is known as the eutectic phase within the Fe-B phase diagram for stable equilibrium. Therefore, the STEM analysis was performed in order to find some precipitates which can contain the Fe_2B intermetallic compound, Fig. 9-12.

The first area evinces the following distribution of the analyzed elements, Fig. 10.

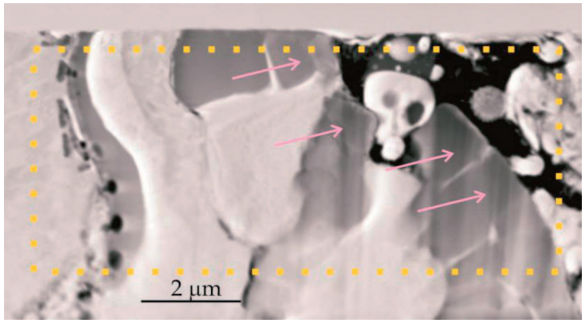

Fig. 9. First area of the Fe-Al coating subjected to the STEM analysis; arrows show the cellular structure

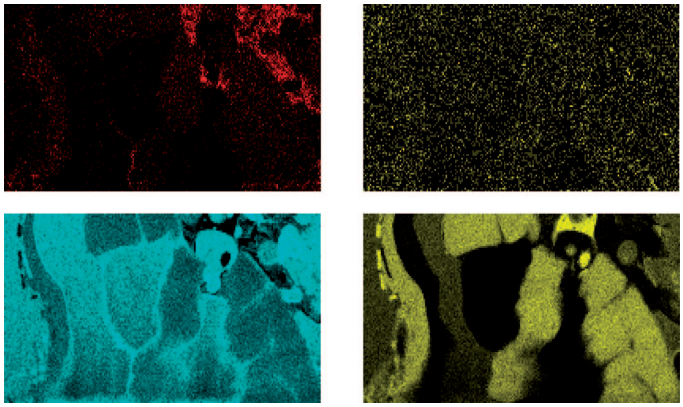

Fig. 10. Distribution of the **B**, **Zr**, **Fe** and **Al** within the analyzed area

According to the performed analysis there is not a significant segregation of Zr, Fig. 10b. However, B is located just ahead of the interface of cells, Fig. 10a. Cells are visible not only in Fig. 9, but in the Fig. 10c and Fig. 10d as well.

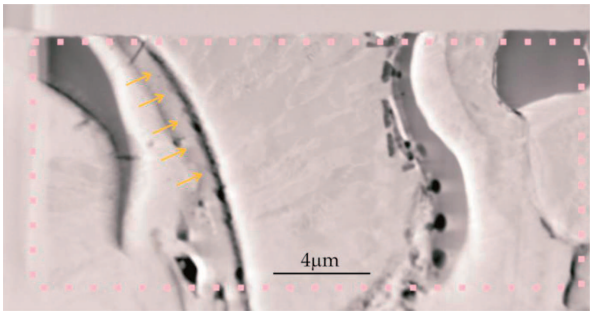

Fig. 11. Second area of the Fe-Al coating subjected to the STEM analysis; arrows show the cellular structure

The second area evinces the following distribution of the analyzed elements, Fig. 12.

According to the performed analysis there is not a significant segregation of Zr, Fig. 12b. However, B is located just ahead of the interface of cells, Fig. 12a. Cells are visible not only in Fig. 11, but in the Fig. 12c and Fig. 12d as well.

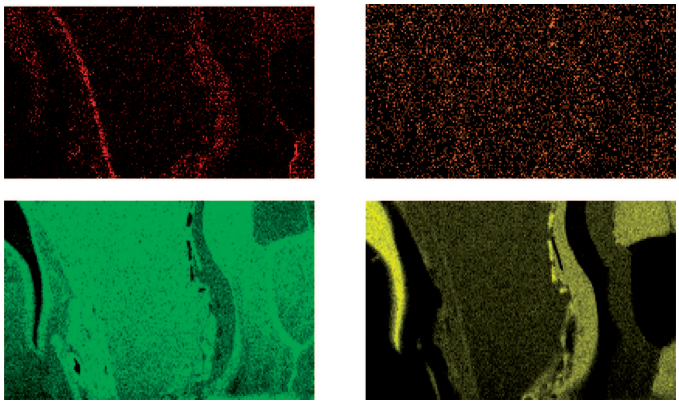

Fig. 12. Distribution of the **B**, **Zr**, **Fe** and **Al** within the analyzed area

3. Model for a single particle solidification

The elements distribution shown in Fig. 10 and Fig. 12 is dealing with the boron, zirconium, aluminum and iron localizations analyzed in the macro scale. The observations in the macro scale confirm also the variety of different structures which are the result of solidification, Fig. 9, Fig. 11. Such a structural analysis is well known, [5], [14], [15], [20]. However, the structure resulting from solidification in the micro scale was not yet analyzed, [14]. Therefore, an attempt is made in the current model to deliver the description of the structure formation within the single Fe-Al particle subjected to solidification during the detonation spraying.

An analyzed particle contained nominally $N_0 = 0.63$, [mole fr. Al] and a small addition of boron and zirconium. The distribution analysis, Fig. 10, Fig. 12 confirms significant segregation of boron just ahead of the interface of some cells which are the result of solidification. Therefore, the current model for a single particle solidification (solidification in the micro scale) is connected additionally with the boron behavior during the sub-layers formation (discussed in Fig. 1d).

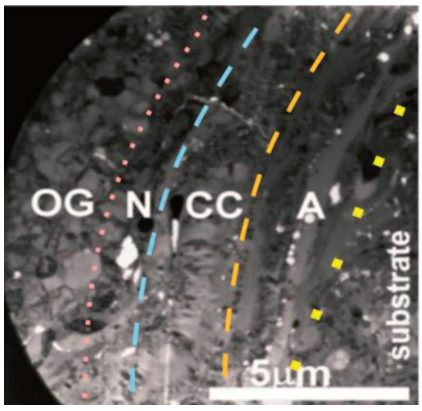

Fig. 13. A separated area which corresponds to the single Fe-Al particle deposited by the D-gun spraying; **OG** = non-melted part of a particle, **N** = a typically non-equilibrium ε_N – phase sub-layer, **CC** = columnar structure of the periodically situated inter-metallic phases (FeAl + Fe_2Al_5) due to the oscillatory mode of solidification, **A** = ε_A amorphous phase sub-layer, **substrate** = a steel substrate

First, the model requires to do an adequate separation (within the Fe-Al coating morphology) of the area which nominally corresponds well to the deposited single Fe-Al particle. Such an area is shown in Fig. 13.

An identification of the phases contained in the considered sub-layers, Fig. 13., was done by means of the TEM study, Fig. 14, Fig. 15.

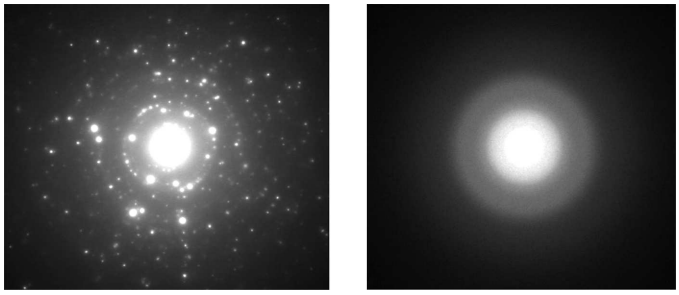

Fig. 14. Identification of some sub-layers phases: a/ε_N – phase, b/ε_A – phase

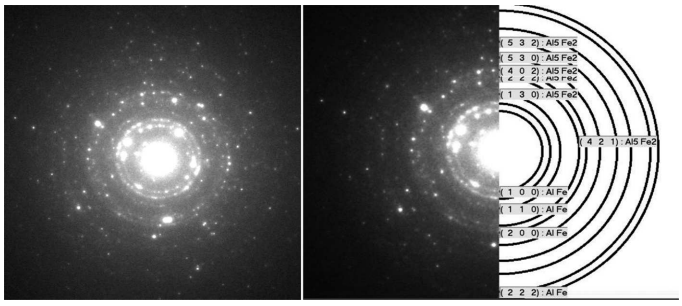

Fig. 15. Identification of the phases (FeAl + Fe_2Al_5) within the **CC** – sub-layer

A single particle transforms its kinetic energy into the heat during the deposition on the steel substrate. Finally, a particle becomes partially melted, then subjected to rapid solidification. Therefore, a non-equilibrium solidification and formation of some meta-stable phases is expected.

The heat transfer occurs in two directions: towards the non-melted part of a particle (next to the air) and towards the substrate. The heat output is significant across the substrate, while the air is not a good thermal conductor. Therefore, solidification occurs under two positive thermal gradients in two directions with different average rates. Thus,

$$G_{AO} >> G_N \quad \text{and} \quad v_{AO} >> v_N \tag{1}$$

where,

G_{AO} – positive (average) thermal gradient at the solid / liquid interface for the ε_A - amorphous phase and the (FeAl + Fe_2Al_5) – phases formation, Fig. 16,

G_N – positive (average) thermal gradient at the solid / liquid interface for the ε_N – non-equilibrium phase formation, Fig. 16,

v_{AO} – solidification rate for the ε_A – amorphous phase and the (FeAl + Fe_2Al_5) – phases formation, Fig. 16.,

v_N – solidification rate for the ε_N – non-equilibrium phase formation, Fig. 16.

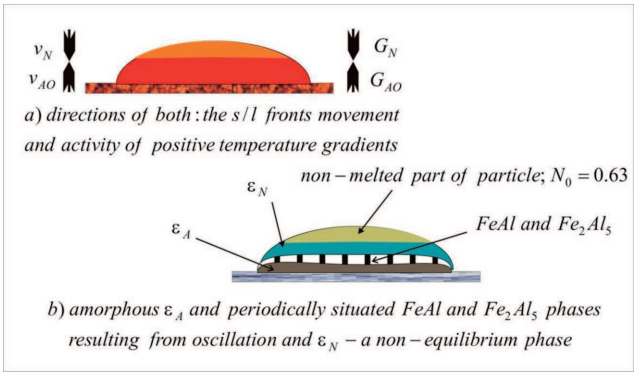

Fig. 16. Model for single particle deposited by D-gun spraying, a/ directions of oriented growth accompanied by the adequate thermal gradients; b/ phases as the solidification product

The identified phases within the sub-layers visible in Fig. 16b were expected according to the localization of the nominal Al-solute concentration, N_0, in the phase diagram for stable equilibrium, Fig. 17.

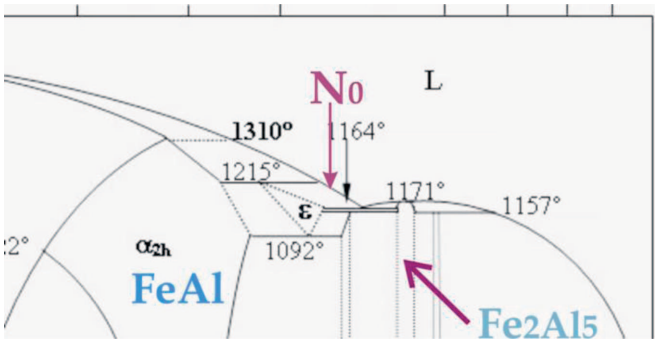

Fig. 17. Localization of the nominal Al-solute concentration N_0 = 0.63 [mole fr.] in the Fe-Al phase diagram for stable equilibrium, [21]

The phase diagram shown in Fig. 17 is useful in explanation of the formation of all the phases visible in the single particle deposited by D-gun spraying, Fig. 16. At first, a model for the typically non-equilibrium ε_N – phase formation is delivered, Fig. 18.

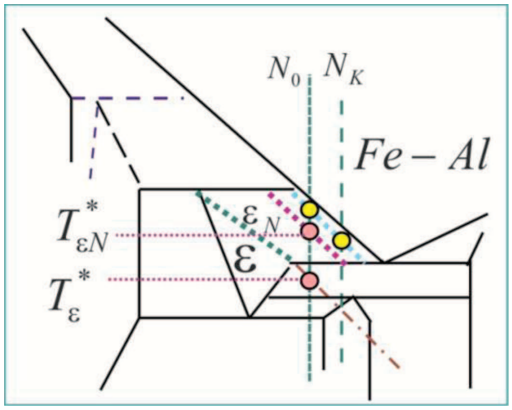

Fig. 18. Field for the appearance of the non-equilibrium ε_N – phase

The equilibrium *solidus* line (dashed green line) for the ε – phase formation is shifted to a new position (dashed violet line) due to the rapid solidification. The equilibrium *liquidus*

line is shifted to a new position (dashed blue line) due to the same reason.

The field between both solidus lines is an area of the ε_N – non-equilibrium phase existence. The movement of the equilibrium lines in the phase diagrams is well defined by the Aziz's theory, [22].

The intersection of the N_0 – solute concentration with the non-equilibrium *liquidus* line determines the beginning of the solidification path, (yellow point). The supposed end of solidification path is shown as the N_K – point (yellow point). Moreover, the N_K – point localization on *liquidus* line can be precisely determined, [23].

The intersection of the N_0 – solute concentration with the non-equilibrium *solidus* line determines the $T^*_{\varepsilon N}$ – temperature of the solid / liquid interface for the ε_N – non-equilibrium phase formation (pink point). The intersection of the N_0 – solute concentration with the meta-stable part of the equilibrium *solidus* line (dotted/dashed line) determines the T^*_{ε} – temperature of the solid / liquid interface for the ε – equilibrium phase formation (pink point). It is evident that the following inequality is satisfied:

$$T^*_{\varepsilon N} > T^*_{\varepsilon} \tag{2}$$

If so, the ε_N – non-equilibrium phase is formed during solidification instead of the ε – equilibrium phase because the ε_N – phase is the winner in the growth competition as it has a higher temperature of its solid / liquid interface, [24].

Model for the ε_N – phase growth within the **N** – sub-layer, Fig. 13, is connected with the activity of the G_N – thermal gradient, Fig. 16a. The ε_N – phase is growing at the average solidification rate equal to v_N, Fig. 16a. The ε_N – phase appears according to the ε_N – phase field defined in Fig. 18 (on the non-equilibrium *solidus* line).

The ε_A – amorphous phase solidifies immediately as the segregationless phase. It is possible when the partition ratio becomes equal to unity, $k = 1$. It means that the *liquidus* and *solidus* lines make the superposition for the rapid solidification, [22].

Usually, the solute segregation / redistribution occurs during solidification, [25]. The adequate differential equation which describes the solute segregation after back-diffusion is as follows, [23]:

$$\frac{dN^L(x;\alpha)}{dx} = \frac{(1-k)\,N^L(x;\alpha)}{1+\alpha\,k\,x-x} \tag{3}$$

The Eq. (3) is a modification of the well known differential equation, [26], written for the solidification during which the back-diffusion does not occur ($\alpha = 0$):

$$\frac{dN^L(x;0)}{dx} = \frac{(1-k)\,N^L(x;0)}{1-x} \tag{4}$$

where, α – back diffusion parameter, [dimensionless], x – amount of the growing crystal, [dimensionless], N^L – solute concentration in the liquid, [mole fr.].

The solution to Eq. (3) describes the solute concentration changes in the liquid:

$$N^L(x;\alpha) = N_0\,(1+\alpha\,k\,x-x)^{(k-1)/(1-\alpha\,k)} \tag{5}$$

for which the solidification path situated on *liquidus* line is:

$$N_0 \rightarrow N_K \tag{5a}$$

Consequentially, the solute segregation at the moving solid / liquid interface is:

$$N^S(x;\alpha) = k\,N_0\,(1+\alpha\,k\,x-x)^{(k-1)/(1-\alpha\,k)} \tag{6}$$

for which the so-called "historical" solid / liquid interface path (segregation path) situated on *solidus* line is:

$$k\,N_0 \rightarrow k\,N_K \tag{6a}$$

Finally, the solute redistribution is given as, [23]:

$$N^B\left(x;X^0,\alpha\right) = \left[k+\beta^{ex}\left(x;X^0\right)\beta^{in}\left(X^0,\alpha\right)\right]N^L(x;\alpha) \tag{7}$$

and the redistribution path is situated just between the solidification path, Eq. (5a) and "historical" solid / liquid interface path (segregation path), Eq. (6a).

In the case of the segregationless formation of the amorphous phase, when the superposition of the *liquidus* and *solidus* lines is required ($k = 1$),

a/ the solute concentration in the liquid does not change (as it results from Eq. (5)),

$$N^L(x;\alpha) \rightarrow N_0 \tag{8a}$$

b/ the solute concentration at the solid / liquid interface does not change (as it results from Eq. (6)),

$$N^S(x;\alpha) \rightarrow N_0 \tag{8b}$$

c/ the solute concentration in the solid does not change (as it results from Eq. (7) for which $\beta^{ex}\left(x;X^0\right) = 0$ when $k = 1$),

$$N^B\left(x;X^0,\alpha\right) \rightarrow N_0 \tag{8c}$$

So, all three paths have been reduced to N_0 solute concentration, (that is to the point). It means that the paths are equal to zero. It can also be concluded that the segregationless / redistributionless solidification (diffusionless solidification) is the particular case of the solidification accompanied by segregation / redistribution. Moreover, it can be concluded that the N_0 – point is the place of the amorphous phase formation when $k = 1$, Fig. 19.

It can be assumed that the superposed *liquidus* and *solidus* lines are additionally juxtaposed by the $T_0(N_0)$ line, Fig. 19. The $T_0(N_0)$ line means the equality of the solid free energy and the liquid free energy. So, it is assumed that the $T_0(N_0)$ is the highest temperature at which solid phase (amorphous phase) can form with the same solute concentration as the liquid.

According to the current model the ε_A – amorphous phase sub-layer is formed at the intersection of the N_0 – solute concentration with the T_0 – line, Fig. 19. In fact, the ε_A – amorphous phase should be formed a little below the intersection point, ***A***, because a certain driving force is necessary to ensure the solidification, [27]. In this case the superposed *liquidus* and *solidus* lines with the ***A*** – intersection point are to be localized below the T_0 – line.

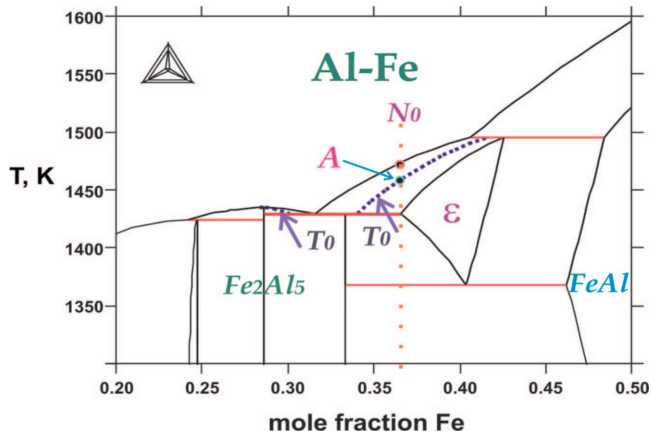

Fig. 19. Juxtaposition of the non-equilibrium *liquidus* and *solidus* lines (superposed each on the other for $k = 1$) by the $T_0\,(N_0)$ – line (as calculated by means of the *Thermocalc Software*); N_0 is the nominal Al-solute concentration of the D-gun deposited Fe-Al particle; ***A*** is the point at which the ε_A – amorphous phase can form within the **A** – sub-layer selected in Fig. 13

A model for the alternately situated phases, (FeAl + Fe_2Al_5), which are visible in the **CC** – sub-layer, Fig. 13, is connected with the oscillatory mode for a structure formation. The oscillatory mode for the structure formation is well known, especially in the case of eutectic transformation, [28], [29].

The partition ratio which was equal to unity, $k = 1$, when the amorphous phase was formed in the **A** – sub-layer, Fig. 13, becomes less than unity, $k < 1$, when the columnar structure appears in the **CC** – sub-layer. The lamellae of the Fe_2Al_5 phase are there situated alternately to the FeAl phase lamellae. However, the Fe_2Al_5 phase appears as the non-equilibrium phase due to the shifted *solidus* line, whereas the FeAl phase forms instead of the ε – phase, Fig. 20. The ε – phase was eliminated by the FeAl phase during oscillatory mode of the

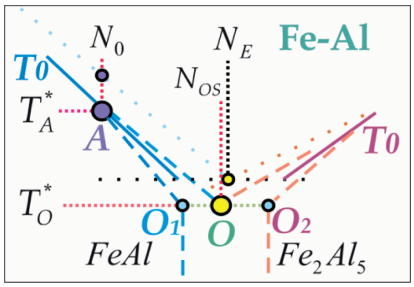

Fig. 20. A part of the Fe-Al phase diagram; a hypothetical localizations of both T_0 – functions are marked by the main lines; the intersection of the N_0 – nominal Al – solute concentration in the considered single particle with the T_0 – function delivers the point at which amorphous phase formation is possible; the dotted lines are the *liquidus* equilibrium lines of the Fe-Al phase diagram for stable equilibrium; the dashed lines describe the diminution of the partition ratio; the diminished partition ratio: $k_{11} = O_1/O$ determines the formation of the meta-stable FeAl – phase and $k_{25} = (1 - O_2)/(1 - O)$ determines the formation of the non-equilibrium Fe_2Al_5 phase

CC – sub-layer formation. Thus, the FeAl phase appears as the meta-stable phase. It is evident that the ε – phase field was eliminated from the Fe-Al phase diagram and the ε – phase field was replaced by the FeAl phase field (in fact, the ε – phase was reduced to the ***A*** – point situated on the superposed *liquidus* and *solidus* lines to form the amorphous phase in the **A** – sub-layer). The amorphous sub-layer was formed first in a sequence, $(T_A^* > T_O^*)$, Fig. 20.

The N_{OS} marked in Fig. 20, is the Al – solute concentration at the oscillatory point ***O***, which corresponds with the N_E – solute concentration at the eutectic point in the phase diagram for stable equilibrium. The ε – phase field is transformed into the ***A*** – point and replaced itself by the FeAl – phase field.

The model for the single particle solidification shown in Fig. 16, is confirmed by some structural observations made in the micro scale, Fig. 21, Fig. 22.

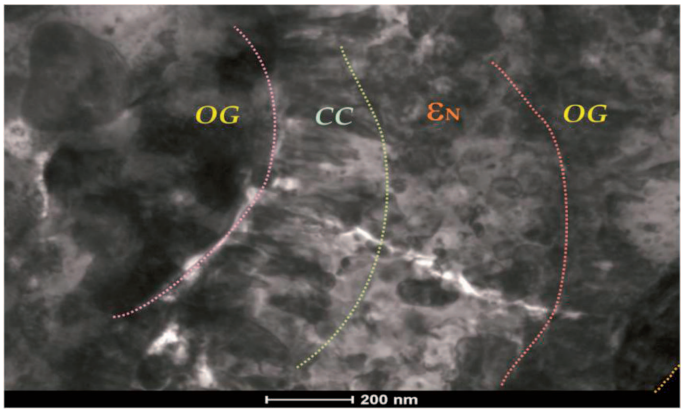

Fig. 21. Experimental confirmation of the model for partially melted single particle solidification; **OG** – non-melted part of the particle deposited formerly (l.h.s. of the morphology); **CC** – alternately situated (FeAl + Fe_2Al_5) – phases; $\varepsilon_{\mathbf{N}}$ – some cells of the non-equilibrium ε_N – phase; **OG** – non-melted part of the observed FeAl particle (r.h.s. of the morphology); the ε_A – amorphous phase of the observed particle is not visible (covered up by the non-melted part of the formerly deposited particle)

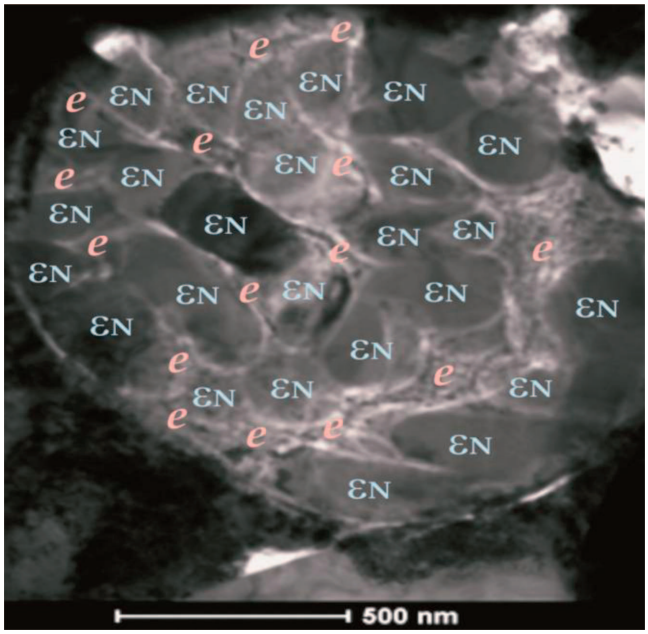

Fig. 22. The $\varepsilon_{\mathbf{N}}$ – sub-layer cross-section, ($\varepsilon_{\mathbf{N}}$ – sub-layer is shown in Fig. 21, formerly named as the **N** – sub-layer, Fig. 13); some cells of the ε_N – phase are well visible; every cell is surrounded by the eutectic precipitate, *e*, in the micro scale (the phenomenon is identical to that revealed in the Fig. 9 and Fig. 11 in the macro scale)

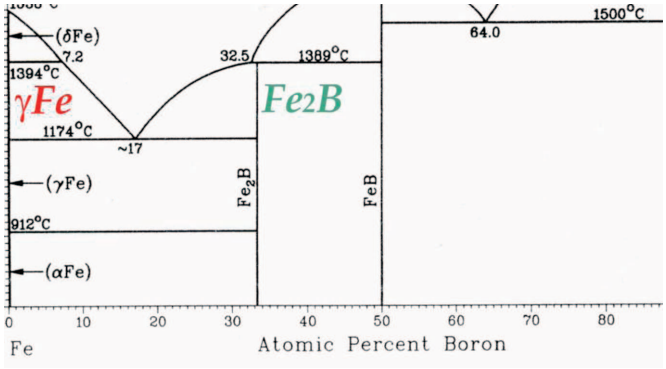

Fig. 23. A part of the Fe-B phase diagram for stable equilibrium, [21]

The appearance of the eutectic precipitate, e, in the grooves between the ε_N – phase cells, Fig. 21, confirms that the solidification path shown in Fig. 18, is as follows: $N_0 \rightarrow N_E$, $(N_K = N_E)$.

Since the boron was revealed in the macro scale just ahead of the arrested solid / liquid interface of the ε_N – phase cells, Fig. 10, Fig. 12, it is postulated that observed precipitate is not only Fe-Al eutectic, Fig. 17, but Fe-B eutectic, Fig. 23, as well. Both investigated eutectics have the similar temperature for transformation ($(\varepsilon$+$Fe_2Al_5) \rightarrow$1171°C, Fig. 17, and (γFe+Fe_2B) $\rightarrow$ 1174°C, Fig. 23). Thus, both eutectics were precipitated practically at the same time. The eutectics were

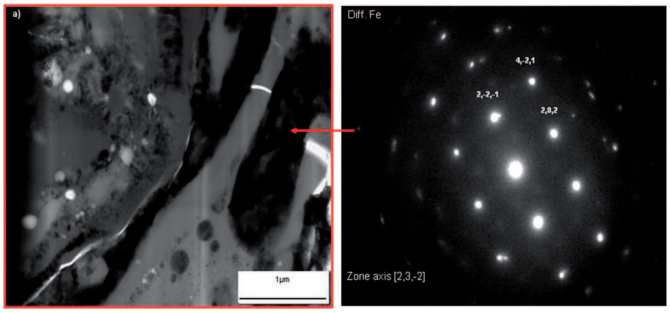

Fig. 24. Identification of the (ε+Fe_2Al_5) – eutectic

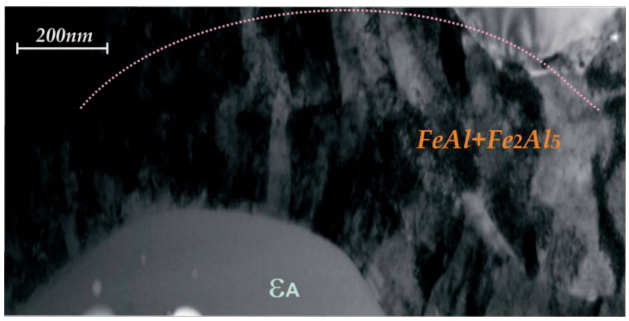

Fig. 25. A boundary between the ε_A – amorphous phase and alternately situated (FeAl + Fe_2Al_5) phases; the (FeAl + Fe_2Al_5) phases were followed the unidirectional solidification perpendicularly / radially to the ε_A – phase surface with the heat transfer through the ε_A – amorphous phase

pushed by the solid / liquid interface of the ε_N – phase cells during their solidification. The (ε+Fe_2Al_5) – eutectic is dominant in this area and therefore was identified easily, Fig. 24.

The single particle morphology revealed in Fig. 25, confirms that the ε_A – amorphous phase and alternately situated (FeAl + Fe_2Al_5) phases appeared sequentially, because $T^*_A > T^*_O$, as it results from the phase diagram shown in Fig. 20.

The subsequent observation of a single particle partially melted during D-gun spraying is presented in Fig. 26. The revealed morphology confirms the model shown in Fig. 16b.

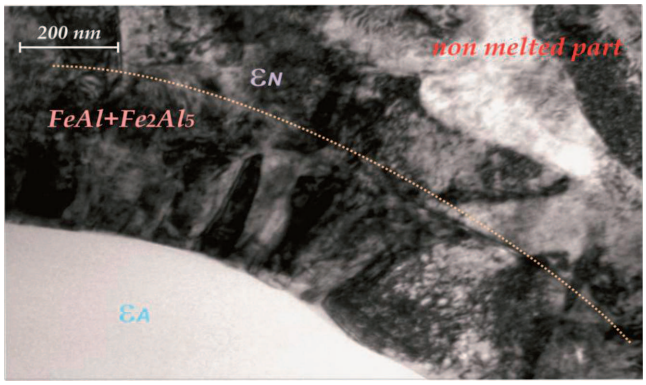

Fig. 26. Morphology of the single Fe-Al particle as deposited by the D-gun spraying; there are visible: the ε_A – amorphous phase in the **A** – sub-layer, the alternately situated (FeAl + Fe_2Al_5) phases in the **CC** – sub-layer, the ε_N – phase in the **N** – sub-layer and non-melted part of the particle in the **OG** – sub-layer

The next observation of the single Fe-Al particle deposited by the D-gun spraying is presented in Fig. 27.

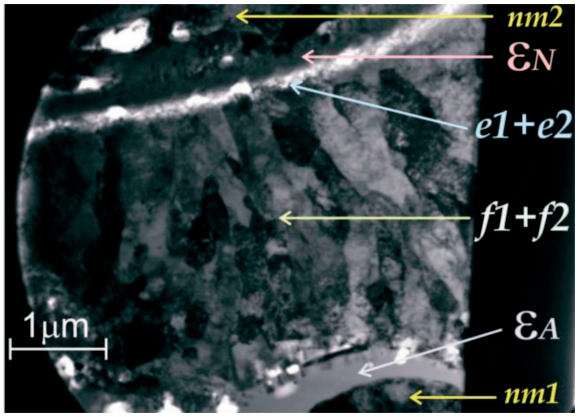

Fig. 27. A single Fe-Al particle as deposited by the D-gun spraying on the steel substrate; $nm1$means a non-melted part of the previously deposited particle in its **OG** – sub-layer, ε_A means the ε – amorphous phase in the **A** – sub-layer, $f1$+$f2$ mean the alternately situated (FeAl + Fe_2Al_5) – phases in the **CC** – sub-layer, respectively, $e1+e2$ mean (ε+Fe_2Al_5) and (γFe+Fe_2B) eutectics as rejected by the solid / liquid interface of the growing ε_N – phase, $nm2$ means a non-melted part of the investigated particle in its **OG** – sub-layer and ε_N means the ε – non-equilibrium phase in the **N** – sub-layer

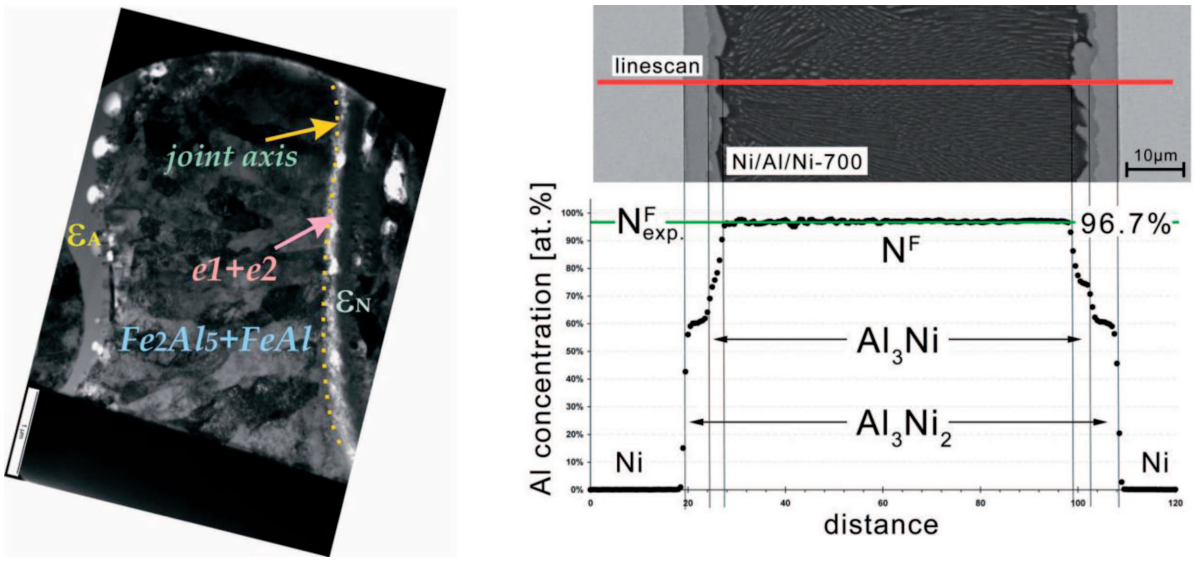

Fig. 28. A diffusion joint a/ in the single Fe-Al particle deposited by D-gun spraying, b/ in the $Ni/Al_3Ni_2/Al_3Ni/N^F/Al_3Ni/Al_3Ni_2/Ni$ interconnection frozen during its isothermal solidification at T = 700°C, [32]; some intermetallic phases / compounds are localized in the both morphologies; the axis is distinguished (dotted yellow line) in the asymmetrical joint created within the single Fe-Al particle; the frozen – not yet solidified foil (with N^F = 0.967 at.% Al) is visible in the middle of a symmetrical diffusion interconnection

The morphology formation in a single particle deposited by the D-gun spraying is similar to the formation of the interconnection during diffusion soldering or brazing, [30]. However, the diffusion soldering / brazing occurs under isothermal conditions, at the constant temperature, and two phenomena are observed: dissolution and solidification, [31], [32]. The morphology formation in a single particle occurs under two different positive thermal gradients and temperature is varying during solidification.

In the case of the single particle solidification a meta-stable phase appears similarly to the diffusion soldering during which a meta-stable phase also forms, [33], [34]. Therefore, the current model for a joint formation during the single particle solidification is similar to the model for joint formation during diffusion soldering / brazing, [35].

It is to be emphasized that some intermetallic phases / compounds are formed in both situations: during solidification of the single particle deposited by D-gun spraying, Fig. 28, and during solidification which occurs in the interconnection produced isothermally by the diffusion soldering / brazing, [30].

The Fe-Al single particle morphology, (micro scale), Fig. 28a, confirms that:

a/ the ε_N- non-equilibrium phase, Fig. 18, was growing with the heat transfer through the non-melted part of the particle,

b/ the ε_N- phase was growing unidirectionally towards the formed joint axis, Fig. 28a,

c/ the average solidification rate was equal to v_N, Fig. 16,

d/the average positive thermal gradient was equal to G_N, Fig. 16,

e/ the ε_A- amorphous phase, Fig. 18, was growing with the heat transfer through the substrate,

f/ the ε_A- phase was solidified immediately due to the diffusionless / segregationless mode of solidification,

g/ the solidification path, the solid / liquid interface path and redistribution path, all together, were equal to zero, Eq. 8, and situated at the intersection of the nominal solute concentration in the single particle, N_0, with the superposed *liquidus* and *solidus* lines, (k = 1), that is at the ***A*** – point for amorphous phase formation, Fig. 19, Fig. 20,

h/ the average positive thermal gradient was equal to G_{AO}, Fig. 16,

i/ the columnar (FeAl + Fe_2Al_5) phases were growing with the heat transfer through the ε_A- amorphous phase,

j/ the columnar (FeAl + Fe_2Al_5) phases were growing unidirectionally towards the formed joint axis, Fig. 28a,

k/ the average solidification rate was equal to v_{AO}, Fig. 16,

l/ the average positive thermal gradient was equal to G_{AO}, Fig. 16,

m/ the solidification was occuring due to oscillatory mode with $k < 1$, Fig. 20,

n/ the formed joint, Fig. 28a is asymmetrical structurally, because $G_{AO} >> G_N$ and in the consequence $v_{AO} >> v_N$, Eq. 1,

o/it is necessary to impose a certain pressure when the diffusion interconnection is formed during isothermal soldering, Fig. 28b,

p/ the pressure is generated by the shock when the single particle beats the substrate, Fig. 1b,

r/ the growing cells of the ε_N- phase pushed both eutectics, (ε+Fe_2Al_5) + (γFe+Fe_2B), then rejected them just at the joint axis, Fig. 28a,

s/ the axis (yellow dotted line) divides the formed interconnection into two parts:

substrate/ε_A/(FeAl + Fe_2Al_5) **and** (ε+Fe_2Al_5) + (γFe+Fe_2B)/ε_N/**non-melted cap**.

4. Concluding remarks

The phenomenological macro / micro modelling was applied to the Fe-Al coating in order to describe the solidifica-

tion of the partially melted single Fe-Al particle deposited by D-gun spraying onto the steel substrate.

The proposed model for a single particle solidification allows for considering the competition between growth of equilibrium ε – phase and non-equilibrium ε_N – phase. The ε_N – phase is the winner in the competition, Fig. 18, and appears within the single particle morphology. On the other side, the proposed model for a single particle solidification shows that the ε_A – amorphous phase and alternately situated (FeAl + Fe_2Al_5) – phases appear sequentially.

The STEM analysis allowed for revealing a localization of zirconium and boron in the macro scale, Fig. 10, Fig. 12. However, the boron segregates significantly just ahead of the interface of cells of the ε_N – phase, only. In the micro scale, the boron precipitates are visible at the joint axis (when a single particle is treated as a diffusion interconnection). The beneficial activity of boron and zirconium for the Fe-Al alloy is well known, [1], [3], [6], [14]. It is considered that boron increases the mechanical properties of the Fe-Al alloys due to its localization at the grains boundaries.

In the case of the analyzed single particle, Fig. 28a, boron is also localized at the cells / columnar structure boundary, (**N / CC**). Therefore, it can be expected that the (γFe+Fe_2B) eutectic improves significantly adhesion of the Fe-Al coating to the steel substrate / Ni-20Cr interlayer system as it was confirmed by mechanical properties investigation, [14]. On the other side, it can be concluded that the exclusive presence of the (ε+Fe_2Al_5) eutectic at the joint axis, Fig. 28a, is not sufficient to ensure the good adhesion. Moreover, the exclusive presence of the (ε+Fe_2Al_5) eutectic at the joint axis, can make weaker a given a single particle treated as an interconnection.

The proposed model is a general one and therefore can be applied to description of Ni/Al/Ni or Ti/Al/Ti multi-layers formation as that observed during the self-propagating high temperature synthesis (SHS).

Acknowledgements

The financial support from National Science Centre – Poland (NCN) through project 2012/05/B/ST8/01794 is gratefully acknowledged.

REFERENCES

[1] K. Niemi, P. Vuoristo, T. Mäntylä, Properties of alumina-based coatings deposited by plasma spray and detonation gun spray processes, Journal of Thermal Spray Technology **3**, 199-203 (1994).

[2] S.C. Deevi, V.K. Sikka, Nickel and iron aluminides: An overview on properties, processing, and applications, Intermetallics **4**, 357-375 (1996).

[3] P. Kratochvil, V. Vodickova, J. Hakl, T. Vlasak, P. Hanus, J. Pesicka, High temperature mechanical properties of Fe28Al4Cr alloy with additives TiB2 and Zr, Intermetallics **18**, 1365-1368 (2010).

[4] W. Hong-Tao, L. Chang-Jiu, Y. Guan-Jun, L. Cheng-Xin, Z. Qiang, L. Wen-Ya, Microstructural characterization of cold-sprayed nanostructured FeAl intermetallic compound coating and its ball-milled feedstock powders, Journal of Thermal Spray Technology **16**, 669-676 (2007).

[5] C. Senderowski, Z. Bojar, Influence of detonation gun spraying conditions on the quality of Fe-Al intermetallic protective coatings in the presence of NiAl and NiCr interlayers, Journal of Thermal Spray Technology **18**, 435-447 (2009).

[6] F. Dobes, J. Pesicka, P. Kratochvil, Creep of the Fe-18Al-4Cr alloy with zirconium addition, Intermetallics **18**, 1353-1356 (2010).

[7] F. Dobes, K. Milicka, Estimation of ductility of Fe-Al alloys be means of small punch test, Intermetallics **18**, 1357-1359 (2010).

[8] D. Vogel, A. Hotar, A. Vogel, M. Palm, F.U. Renner, Corrosion behaviour of Fe-Al(-Ti) alloys in steam, Intermetallics **18**, 1375-1378 (2010).

[9] P. Hanus, E. Bartsch, M. Palm, R. Krein, K. Bauer-Partenheimer, P. Janschek, Mechanical properties of a forged fe-25Al-2Ta steam turbine blade, Intermetallics **18**, 1379-1384 (2010).

[10] A. Hotar, M. Palm, Oxidation resistance of the Fe-25Al-2Ta (at.%) in air, Intermetallics **18**, 1390-1395 (2010).

[11] T. Skiba, P. Hausild, M. Karlik, K. Vanmeensel, J. Vleugels, Mechanical properties of spark plasma sintered FeAl intermetallics, Intermetallics **18**, 1410-1414 (2010).

[12] R. Musalek, O. Kovarik, T. Skiba, P. Hausild, M. Karlik, J. Colmenares-Angulo, Fatigue properties of Fe-Al intermetallic coatings prepared by plasma spraying, Intermetallics **18**, 1415-1418 (2010).

[13] C. Senderowski, Z. Bojar, W. Wołczyński, G. Roy, T. Czujko, Residual stresses determined by the modified Sachs method within a gas detonation sprayed coatings of the Fe-Al intermetallic, Archives of Metallurgy and Materials **52**, 569-578 (2007).

[14] G. Ji, T. Grosdidier, N. Bozzolo, S. Launois, The mechanisms of microstructure formation in a nanostructured oxide dispersion strengthened FeAl alloy obtained by spark plasma sintering, Intermetallics **15**, 109-118 (2007).

[15] C. Senderowski, Z. Bojar, W. Wołczyński, A. Pawłowski, Microstructure characterization of D-gun sprayed Fe-Al intermetallic coatings, Intermetallics **18**, 1405-1409 (2010).

[16] C. Senderowski, A. Pawłowski, Z. Bojar, W. Wołczyński, M. Faryna, J. Morgiel, Ł. Major, TEM microstructure of Fe-Al coatings detonation sprayed onto steel substrate, Archives of Metallurgy and Materials **55**, 373-381 (2010).

[17] A. Pawłowski, C. Senderowski, W. Wołczyński, J. Morgiel, Ł. Major, Detonation deposited Fe-Al coatings Part II: Transmission electron microscopy of interlayers and Fe-Al intermetallic coating detonation sprayed onto the 045 steel substrate, Archives of Metallurgy and Materials **56**, 71-79 (2011).

[18] K. Vanmeensel, A. Laptev, J. Hennicke, J. Vleugels, O. Van der Biest, Modelling of the temperature distribution during field assisted sintering, Acta Materiallia **53**, 4379-4388 (2005).

[19] U. Anselmi-Tamburini, S. Gennari, J.E. Garay, Z.A. Munir, Fundamental investigations on the spark plasma sintering / synthesis process – II. Modelling of current and temperature distributions, Materials Science and Engineering **394A**, 139-148 (2005).

[20] A. Pawłowski, C. Senderowski, Z. Bojar, M. Faryna, Detonation deposited Fe-Al coatings part I: Morphology of Ni(Al) and Cr(Ni) transition layers and coatings of Fe-Al type sprayed onto carbon steel substrate, Archives of Metallurgy and Materials **55**, 1061-1071 (2010).

[21] O. Kubaschewski, IRON – Binary Phase Diagrams, Springer-Verlag, Berlin, Heidelberg, New York, 1982.

[22] M.J. Aziz, Model for solute redistribution during rapid solidification, Journal of Applied Physics **53**, 1158-1168 (1982).

[23] W. Wołczyński, Back-diffusion phenomenon during the crystal growth by the Bridgman method, Chapter 2. in: Modelling of Transport Phenomena in Crystal Growth, p. 19-59, WIT Press, Southampton (UK) – Boston (USA), 2000, eds J.Szmyd & K.Suzuki.

[24] T. Umeda, T. Okane, W. Kurz, Phase selection during solidification of peritectic alloys, Acta Materiallia **44**, 4209-4216 (1996).

[25] W. Wołczyński, J. Kloch, Solute redistribution after back-diffusion in cellular and dendritic growth of binary alloys, Bulletin of the Polish Academy of Sciences; Technical Sciences **46**, 277-288 (1998).

[26] E. Scheil, Über die eutektische kristallization, Zeitschrift für Metallkunde **34**, 70-80 (1942).

[27] J. Dutkiewicz, T.B. Massalski, Search for metallic g lasses in the Ag-Cu-Ge, Ag-Cu-Sb and Ag-Cu-Sb-Ge systems, Metallurgical Transactions **12A**, 773-778 (1981).

[28] G. Boczkal, B. Mikułowski, W. Wołczyński, Oscillatory structure of the Zn-Cu-Ti single crystals, Materials Science Forum **649**, 113-118 (2010).

[29] W. Wołczyński, Concentration micro-field for lamellar eutectic growth. Defect and Diffusion Forum **272**, 123-138 (2007).

[30] W. Wołczyński, E. Guzik, J. Janczak-Rusch, D. Kopyciński, J. Golczewski, H.M. Lee, J. Kloch, Morphological characteristics of multi-layer / substrate systems, Materials Characterization **56**, 274-280 (2006).

[31] W. Wołczyński, T. Okane, C. Senderowski, D. Zasada, B. Kania, J. Janczak-Rusch, Thermodynamic justification for the Ni/Al/Ni joint formation by a diffusion brazing, International Journal of Thermodynamics **14**, 97-105 (2011).

[32] W. Wołczyński, J. Kloch, J. Janczak-Rusch, K. Kurzydłowski, T. Okane, Segregation profiles in diffusion soldered Ni/Al/Ni interconnections, Materials Science Forum **508**, 385-392 (2006).

[33] W. Wołczyński, T. Okane, C. Senderowski, B. Kania, D. Zasada, J. Janczak-Rusch, Meta-stable conditions of diffusion brazing, Archives of Metallurgy and Materials **56**, 311-323 (2011).

[34] W. Wołczyński, Transition phenomena in the diffusion soldering / brazing. Archives of Metallurgy and Materials **51**, 609- 615 (2006).

[35] W. Wołczyński, J. Janczak-Rusch, J. Kloch, T. Rutti, T. Okane, A model for solidification of intermetallic phases from Ni-Al system and its application to diffusion soldering, Archives of Metallurgy and Materials **50**, 1055-1068 (2005).

Received: 10 February 2013.